


 Cite this: *RSC Adv.*, 2024, 14, 7499

# The discrepancy of NH<sub>3</sub> oxidation mechanism between SAPO-34 and Cu/SAPO-34

 Xiubin Ren,<sup>a</sup> Yingfeng Duan,<sup>\*a</sup> Wei Du,<sup>\*b</sup> Youyu Zhu,<sup>a</sup> Lina Wang,<sup>a</sup> Yagang Zhang<sup>a</sup> and Tie Yu<sup>ID c</sup>

The difference of NH<sub>3</sub> oxidation mechanism over SAPO-34 and Cu–SAPO-34 was studied. XRD (X-ray diffraction), SEM (scanning electron microscopy) and H<sub>2</sub>-TPR (H<sub>2</sub>-temperature programmed desorption) were conducted to estimate the Cu species distribution. The quantity of individual Cu<sup>2+</sup> ions escalated with the elevation of silicon content in the Cu/SAPO-34 catalysts, leading to an enhancement in the activity of the NH<sub>3</sub>-SCR (ammonia-selective catalytic reduction) process. This augmentation in activity can be attributed to the increased presence of isolated Cu<sup>2+</sup> species, which are pivotal in facilitating the catalytic reaction. In addition, the kinetic test of NH<sub>3</sub> oxidation indicated that the CuO species were the active sites for NH<sub>3</sub> oxidation. Specifically, the strong structural Brønsted acid sites were the NH<sub>3</sub> oxidation active sites over the SAPO-34 support, and the NH<sub>3</sub> reacted with the O<sub>2</sub> on the Brønsted acid sites to produce the NO mainly. While the NH<sub>3</sub> oxidation mechanism over Cu/SAPO-34 consisted of two steps: firstly, NH<sub>3</sub> reacted with O<sub>2</sub> on CuO sites or residual Brønsted acid sites to form NO as the product; subsequently, the generated NO was reduced by NH<sub>3</sub> into N<sub>2</sub> on isolated Cu<sup>2+</sup> sites. Simultaneously, the isolated Cu<sup>2+</sup> sites might demonstrate a significant function in the NH<sub>3</sub> oxidation process to form N<sub>2</sub>. The identification of active sites and corresponding mechanism could deepen the understanding of excellent performance of NH<sub>3</sub>-SCR over the Cu/SAPO-34 catalyst at high temperature.

 Received 10th January 2024  
 Accepted 26th February 2024

DOI: 10.1039/d4ra00248b

[rsc.li/rsc-advances](https://rsc.li/rsc-advances)

## 1. Introduction

Diesel and lean-burn engines are growing in popularity worldwide, due to their superior fuel efficiency and power density, compared to other conventional on-road propulsion sources. However, the abatement of nitrogen oxides (NO<sub>x</sub>) and particulate matter (PM) emissions from exhaust gases of diesel and lean-burn gasoline engines represents a significant challenge for the further development of these vehicles. Among potentially implementable technologies, the selective catalytic reduction of NO<sub>x</sub> using ammonia as reducing agent (NH<sub>3</sub>-SCR) is a well established DeNO<sub>x</sub> technique because of its high efficiency and desired selectivity of N<sub>2</sub>.<sup>1</sup> Several Cu-based zeolite catalysts, such as Cu/ZSM-5 and Cu/beta, perform high NH<sub>3</sub>-SCR activities,<sup>2–5</sup> but the narrow activity window and weak hydrothermal stability impede their commercial applications. The stringent emission regulations lead to the development of aftertreatment systems combining Diesel Particulate Filters (DPF) with highly stable zeolite-based SCR catalysts, capable of withstanding active DPF

regeneration conditions.<sup>6</sup> From these points of view, it is mandatory to develop the hydrothermally stable zeolite materials for SCR application.

The Cu/SAPO-34 catalyst with chabazite (CHA) structure has received great attention on account of its excellent NH<sub>3</sub>-SCR performance and good thermal stability.<sup>7–10</sup> Magdalena found that the ion-exchanged Cu/SAPO-34 catalyst performed high SCR activity between 150 °C and 500 °C, and it was more hydrothermally stable than the Cu–ZSM-5.<sup>11</sup> In our previous researches,<sup>12</sup> it was reported that the isolated Cu<sup>2+</sup> species displaced in the cavity of SAPO-34 were the active sites for the NH<sub>3</sub>-SCR reaction at low temperature. In addition, it was also found that the NO conversion of Cu/SAPO-34 catalyst started to decrease slightly above 300 °C, while the NH<sub>3</sub> conversion kept increasing till 100%.<sup>13</sup> It is known that the NH<sub>3</sub> oxidation at high temperature could compete with NH<sub>3</sub>-SCR reaction and inhibit the NO conversion. On the other hand, in the practical aftertreatment system of diesel, the NH<sub>3</sub> oxidation catalyst is always set after the SCR catalyst to eliminate the NH<sub>3</sub> slip.<sup>14–16</sup> If the Cu/SAPO-34 catalyst concurrently performs superior SCR and NH<sub>3</sub> oxidation activity, the NH<sub>3</sub> oxidation catalyst can be omitted for economic effect. Therefore, the exploration of mechanisms referring to the NH<sub>3</sub>-SCR, NH<sub>3</sub> oxidation and their competition is meaningful and necessary for further developing the efficient SCR catalyst.

Additionally, previous researches had revealed that the hydrothermal treatment could manipulate Cu species distribution on frameworks of Cu/SAPO-34 catalysts, and the

<sup>a</sup>School of Chemistry and Chemical Engineering, Xi'an University of Science and Technology, Xi'an 710054, PR China. E-mail: xustduanyf@xust.edu.cn

<sup>b</sup>School of Chemical Engineering, Xi'an University, Xi'an 710065, PR China. E-mail: duwei0201@xawt.edu.cn

<sup>c</sup>Institute of Molecular Science and Engineering, Shandong University, Shandong 266237, PR China


change of Cu species distribution further influenced their SCR activity and N<sub>2</sub> selectivity.<sup>17–20</sup> However, the distribution of Cu species can also influence the NH<sub>3</sub> oxidation activity, which has not been studied in detail yet. Therefore, in present work, we synthesized the Cu/SAPO-34 catalyst by the impregnation method to ensure that CuO was the dominated Cu species. And the various Cu species distributions were achieved *via* the control of acidity on SAPO-34 supports on the conditions of comparable Cu loading. The structure and Cu species distribution were characterized by XRD, SEM and H<sub>2</sub>-TPR. Concurrently, the NH<sub>3</sub>-SCR and NH<sub>3</sub> oxidation activities were also evaluated to investigate the effect of Cu species migration on them. Moreover, the kinetic NH<sub>3</sub> oxidation was performed to gain insights into the active sites and the mechanism of the NH<sub>3</sub> oxidation. Finally, this study could also give the guidance to design the optimal Cu/SAPO-34 catalysts to accomplish desired NH<sub>3</sub>-SCR and NH<sub>3</sub> oxidation performance with N<sub>2</sub> as main products.

## 2. Experimental

### 2.1 Catalysts preparation

H-SAPO-34 was synthesized by the hydrothermal method from a gel with a molar composition of 1.0Al<sub>2</sub>O<sub>3</sub>:1.0P<sub>2</sub>O<sub>5</sub>:(0.2–0.8)SiO<sub>2</sub>:2.0morpholine:60H<sub>2</sub>O. The sources of aluminium, phosphorus and silicon were pseudoboehmite, orthophosphoric acid and silica sol, respectively. And the detailed synthesis procedure was presented in our previous work.<sup>13</sup> Three SAPO-34 supports were obtained *via* control of the SiO<sub>2</sub> contents.

The impregnated Cu/SAPO-34 was prepared through two steps. Firstly, H-SAPO-34 and 27 wt% ammonium nitrate solution were mixed and stirred vigorously at 80 °C for 3 h followed by filtering with deionized water. After that the powder was dried at 90 °C for 16 h in the oven to obtain NH<sub>4</sub>/SAPO-34. Secondly, the NH<sub>4</sub>/SAPO-34 was impregnated with the solution of Cu(CH<sub>3</sub>COO)<sub>2</sub> as the precursor at room temperature. Then, the impregnated powder was dried at 100 °C for 12 h and calcined at 550 °C in air for 4 h.

The Al, Si, P contents were determined by X-ray Fluorescence (XRF) and the Cu loadings in the catalysts were measured by Inductively Coupled Plasma (ICP) in Table 1. The SAPO-34 supports were abbreviated to “Six”, and the Cu-SAPO-34 catalysts were denoted as “Cu/Six”, where the *x* stand for “the material SiO<sub>2</sub>/Al<sub>2</sub>O<sub>3</sub> ratio”.

### 2.2 Activity tests

The activity tests were performed in a quartz reactor at atmospheric pressure, using 100 mg sample (60–80 mesh) sufficiently mixed with 900 mg quartz (60–80 mesh). The temperature was controlled by a type K thermocouple inserted into the center of the mixed sample. The concentration of NO and NH<sub>3</sub> was monitored by a Fourier transform infrared (FTIR) spectrometer (MKS-2030) equipped with a 5.11 m gas cell, which operating pressure and temperature is 190 °C and 920 torr. The gas flow rates in all experiments were controlled at 500 mL min<sup>-1</sup> by mass flow controllers. Prior to the experiments, the catalysts were pre-treated at 500 °C for 30 min under 5% O<sub>2</sub>/N<sub>2</sub>.

The steady-state NH<sub>3</sub> oxidation activity tests were performed using a feed gas composition of 500 ppm NH<sub>3</sub> and 5% O<sub>2</sub> with N<sub>2</sub> as the balance. The tested temperature range was from 200 °C to 550 °C at 50 °C intervals. The NH<sub>3</sub> conversion was calculated using the following equation:

$$\text{NH}_3 \text{ conversion } [\%] = \frac{\text{NH}_3 \text{ inlet} - \text{NH}_3 \text{ outlet}}{\text{NH}_3 \text{ inlet}} \times 100 [\%] \quad (1)$$

Steady-state activity tests were also performed for the NH<sub>3</sub>-SCR activity tests, using the gas composition of 500 ppm NO, 500 ppm NH<sub>3</sub> and 5% O<sub>2</sub> with N<sub>2</sub> as the balance. The tested temperature range was from 120 °C to 600 °C. The NO conversion was calculated using the following equation:

$$\text{NO conversion } [\%] = \frac{\text{NO}_{\text{inlet}} - \text{NO}_{\text{outlet}}}{\text{NO}_{\text{inlet}}} \times 100 [\%] \quad (2)$$

### 2.3 Kinetic measurements

The NH<sub>3</sub> oxidation kinetic tests were performed in a differential reactor, using 25 mg (80–100 mesh) catalyst mixed with 100 mg quartz sands (80–100 mesh). The gas flow rates were controlled at 1500 mL min<sup>-1</sup> and the volume hourly space velocity was 3 600 000 h<sup>-1</sup>. The samples were pre-treated in 5% O<sub>2</sub>/N<sub>2</sub> at 500 °C for 30 min before the kinetic experiments. The kinetic steady-state measurements with a gas composition of 500 ppm NH<sub>3</sub>, 5% O<sub>2</sub> were performed from 380 °C to 480 °C at 20 °C intervals and the NH<sub>3</sub> conversions were controlled less than 20%. The NH<sub>3</sub> oxidation reaction rates were calculated from the NH<sub>3</sub> conversion as the eqn (3):

$$\text{Rate } [\text{mol NH}_3 \text{ per g}_{\text{cata}} \text{ per s}] = \frac{X_{\text{NH}_3} [\%] \times F_{\text{NH}_3} [\text{L}_{(\text{NH}_3)} \text{ min}^{-1}]}{m_{\text{cata}} [\text{g}] \times 60 [\text{s min}^{-1}] \times 22.4 [\text{L mol}^{-1}]} [\text{mol NH}_3 \text{ per g}_{\text{cata}} \text{ per s}] \quad (3)$$

$X_{\text{NH}_3}$  = NH<sub>3</sub> conversion, [%];

$F_{\text{NH}_3}$  = flow rate of NH<sub>3</sub>, [L<sub>(NH<sub>3</sub>)</sub> min<sup>-1</sup>]



Table 1 The composition of SAPO-34 supports and Cu/SAPO-34 catalysts

Supports	Material ratios	Al/Si/P molar ratio	Corresponding catalysts	Cu loading (wt%)
Si0.2	1 : 1 : 0.2	$\text{Si}_{0.064}\text{Al}_{0.486}\text{P}_{0.450}\text{O}_2$	CuSi0.2	0.76
Si0.4	1 : 1 : 0.4	$\text{Si}_{0.107}\text{Al}_{0.492}\text{P}_{0.401}\text{O}_2$	CuSi0.4	0.98
Si0.8	1 : 1 : 0.8	$\text{Si}_{0.125}\text{Al}_{0.467}\text{P}_{0.408}\text{O}_2$	CuSi0.8	0.74

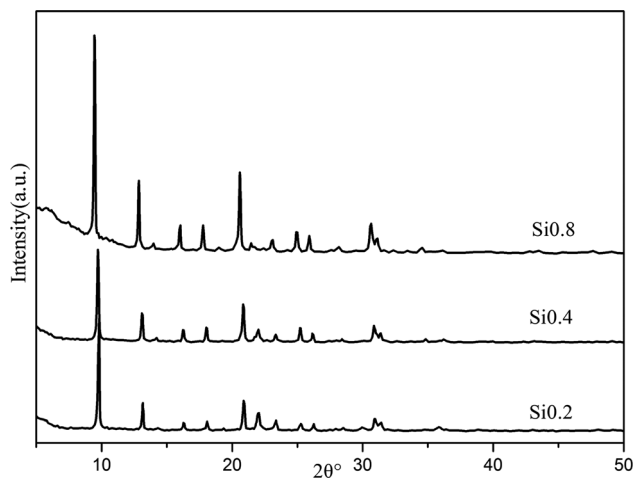


Fig. 1 The XRD profiles of the SAPO-34 supports.

## 2.4 Characterization of the catalysts

The scanning electron microscopy (SEM) image of the samples was measured on a HITACHI S4800 field emission microscope. Before the scanning, the samples were pasted on a carbon tape and covered with Au powder to make it conductive. The structures of the samples were determined by X-ray diffraction (XRD, Bruker D8 Advance TXS, Cu K $\alpha$  radiation). The XRD pattern was collected with a step size of 0.02° from 5° to 50°.

Temperature-programmed reduction by hydrogen experiment (H<sub>2</sub>-TPR) was performed to characterize the reducibility of various copper species in the Cu/SAPO-34. Prior to the reduction, the samples (100 mg) were pre-treated at 500 °C under 2% O<sub>2</sub>/N<sub>2</sub> (30 mL min<sup>-1</sup>) for 1 h. Then after cooling down, the samples were elevated at a ramping rate of 10 °C min<sup>-1</sup> from 30 °C to 850 °C under a flow of 5% H<sub>2</sub>/N<sub>2</sub> (30 mL min<sup>-1</sup>). The consumption of hydrogen was monitored by the thermal conductivity detector (TCD).

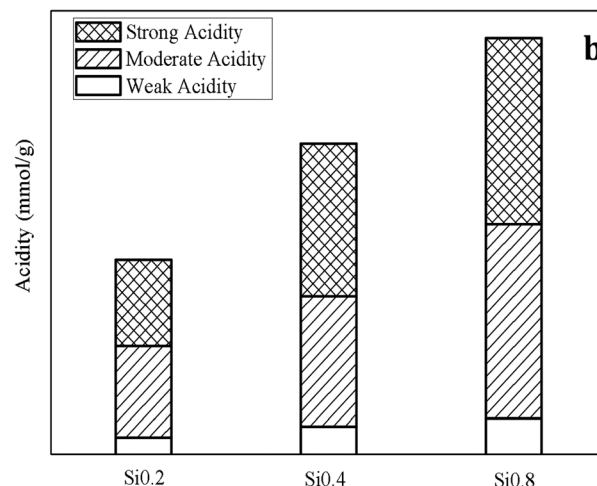
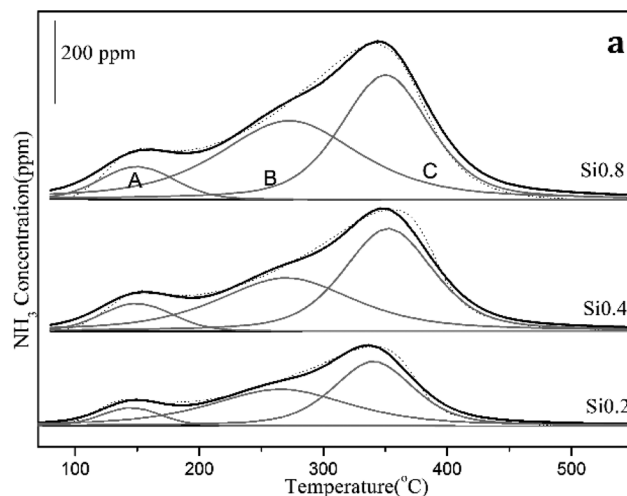
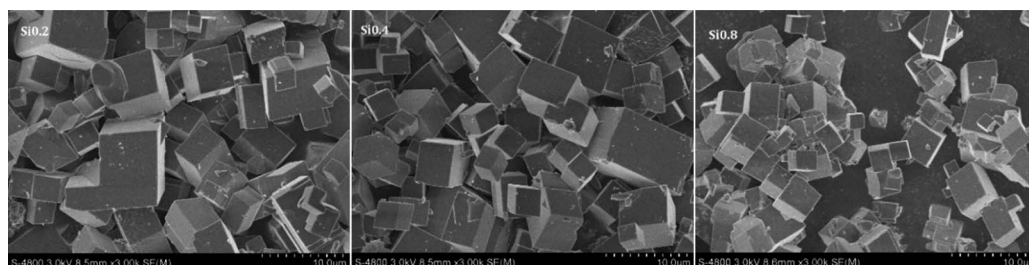
Fig. 3 The NH<sub>3</sub>-TPD profiles and the acid contents for the SAPO-34 supports.

Fig. 2 The SEM images of the SAPO-34 supports.



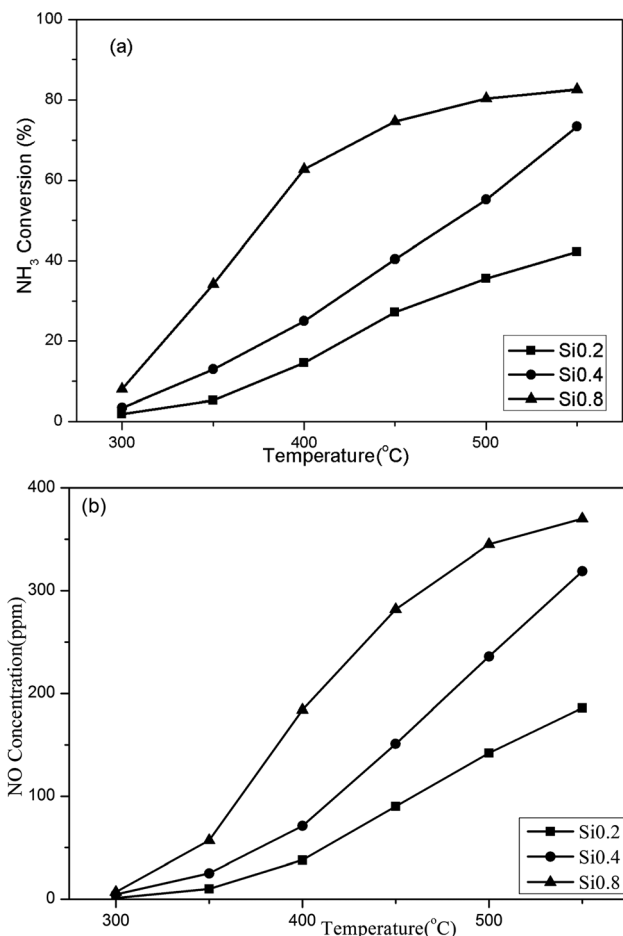


Fig. 4 NH<sub>3</sub> oxidation activities over the SAPO-34 supports. (a) The NH<sub>3</sub> conversion; (b) the NO conversion. The inlets consisted of 500 ppm NH<sub>3</sub> and 5% O<sub>2</sub>, with N<sub>2</sub> as the balance. The volume hourly space velocity in the experiments was kept at 30 000 h<sup>-1</sup>.

Temperature programmed desorption by NH<sub>3</sub> (NH<sub>3</sub>-TPD) experiment was performed to evaluate the acid content of the samples. The catalysts were pretreated at 500 °C for 30 min in

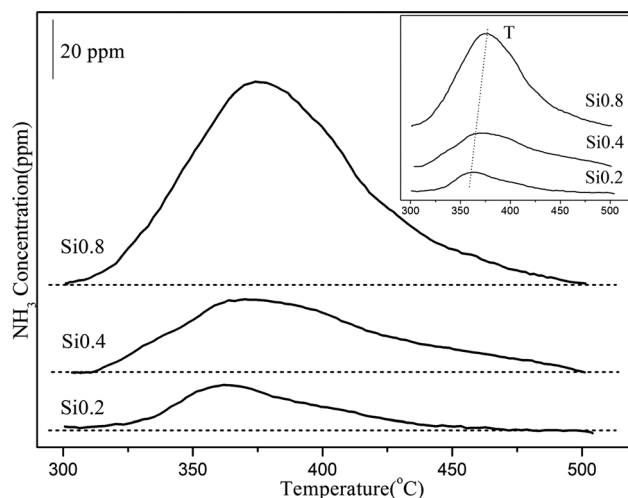


Fig. 5 The NH<sub>3</sub>-TPD profiles of the SAPO-34 supports at 300 °C.

Table 2 Acidity of the supports obtained from NH<sub>3</sub>-TPD at 300 °C

Support	Acidity (mmol g <sup>-1</sup> )
Si0.2	0.0043
Si0.4	0.0091
Si0.8	0.0197

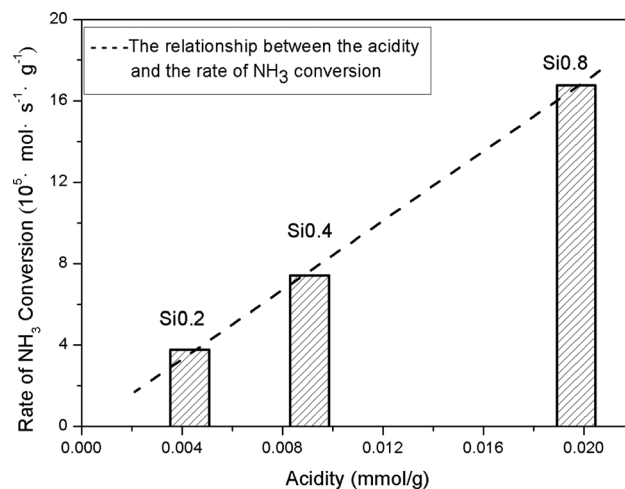


Fig. 6 The relationship between the acidity and the NH<sub>3</sub> conversion rate at 300 °C.

5% O<sub>2</sub>/N<sub>2</sub>, then cooled to and kept at a certain temperature in N<sub>2</sub> before the experiments. NH<sub>3</sub> adsorption was in 500 ppm NH<sub>3</sub>/N<sub>2</sub> until the outlet NH<sub>3</sub> concentration remained unchanged. Then the catalysts were purged with N<sub>2</sub> to remove the weakly absorbed NH<sub>3</sub>. Finally, the catalysts were heated from the certain temperature to 550 °C at a ramping rate of 10 °C min<sup>-1</sup>.

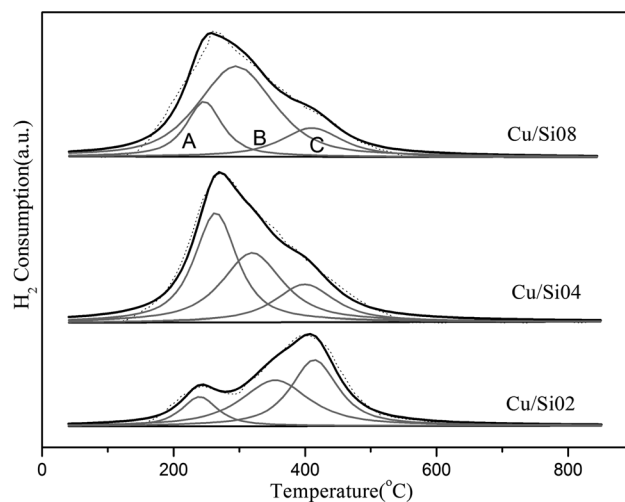


Fig. 7 The H<sub>2</sub>-TPR results for Cu/SAPO-34. Dashed line represents the fitting results.



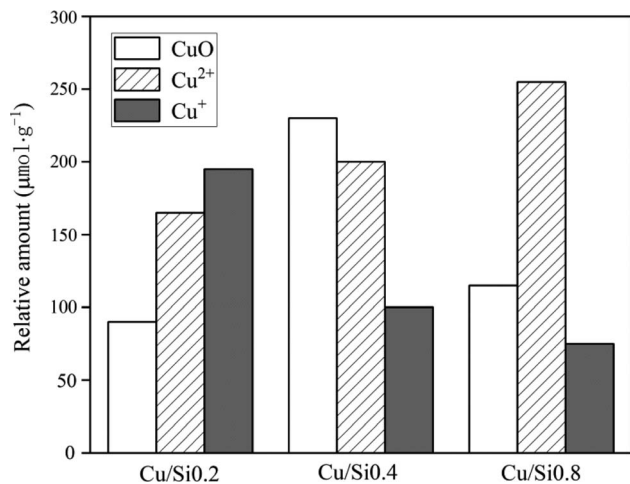


Fig. 8 The relative amount of CuO, isolated Cu<sup>2+</sup> ions and Cu<sup>+</sup> on three catalysts quantified by the H<sub>2</sub>-TPR profile.

## 3. Results and discussion

### 3.1 The NH<sub>3</sub> oxidation over the SAPO-34 supports

**3.1.1 XRD and SEM results.** The XRD profiles in Fig. 1 showed that the three SAPO-34 supports all exhibited typical CHA structure.<sup>21,22</sup> The two main peaks of Fig. 1 ( $2\theta = 9.54^\circ$  and  $20.55^\circ$ ) are assigned to the typical *hkl* miller indexes (100) and (20-1) of SAPO-34 structure (JCPDS 01-087-1527), respectively.<sup>23,24</sup> Moreover, the XRD peaks intensity of three samples increased slightly with the growth of the Si content, which could be attributed to the improvement of its crystallinity. The SEM images of the SAPO-34 supports in Fig. 2 demonstrated that all the samples possessed typical cubic crystals and the crystal sizes were 2–6 μm, which was consistent with the XRD results.

**3.1.2 NH<sub>3</sub>-TPD results.** NH<sub>3</sub>-TPD was conducted to examine the acidities of SAPO-34 supports. As shown in Fig. 3a, the SAPO-34 supports contained three NH<sub>3</sub> desorption peaks,

labelled as A, B and C. Peak A at 150 °C was assigned to the weak Brønsted acid sites at the surface hydroxyl groups. The two peaks (B and C) at higher temperature were assigned to the moderate/strong structural Brønsted acid sites. The protonic acidity of SAPO-34 resulted from the Si incorporation into the neutral framework of AlPOs molecular sieves and the compensation for the unbalanced electronic charges. Therefore, as shown in Fig. 3b, the acid contents of SAPO-34 supports were improved with the increase of the Si content. Moreover, the strong, moderate and weak acid contents all showed the rising trend.

### 3.1.3 The effect of the acidities on NH<sub>3</sub> oxidation at high temperature

(1) *The NH<sub>3</sub> oxidation activity over the H/SAPO-34 supports.* As shown in Fig. 4, the NH<sub>3</sub> conversions over three samples were all below 10% at low temperature, but increased continuously above 300 °C. The increased acidities of the SAPO-34 support directly resulted in an elevated NH<sub>3</sub> oxidation activity. The Si0.8 sample performed the highest NH<sub>3</sub> conversion, while the Si0.2 showed an inferior NH<sub>3</sub> conversion. The main product NO exhibited the same trend as the NH<sub>3</sub> conversion. What is more, the NO<sub>2</sub> and N<sub>2</sub>O concentrations were all below 3 ppm, which were not the main products for NH<sub>3</sub> oxidation and would not affect the determination of N<sub>2</sub> concentration.

(2) *The relationship between the acidities and the NH<sub>3</sub> oxidation activities.* It is well established that the acidity of the catalyst plays a pivotal role in the ammoxidation reaction. Certainly, the increasement in acidity is beneficial for enhancing the performance of catalysts, which profit from that critical NH<sub>3</sub> adsorption process can occur on the catalyst surface in the form of either NH<sub>4</sub><sup>+</sup> on Brønsted acid sites or coordinatively adsorbed NH<sub>3</sub> on Lewis acid sites.<sup>25,26</sup> Since the NH<sub>3</sub> oxidation activity started from 300 °C, the NH<sub>3</sub>-TPD experiment with ammonia adsorption under 300 °C was conducted to further quantitatively estimate the contribution of acidities to the NH<sub>3</sub> oxidation. As shown in Fig. 5 and Table 2, there was only one NH<sub>3</sub> desorption peak from 300 °C to 500 °C for the three supports and the peak area increased

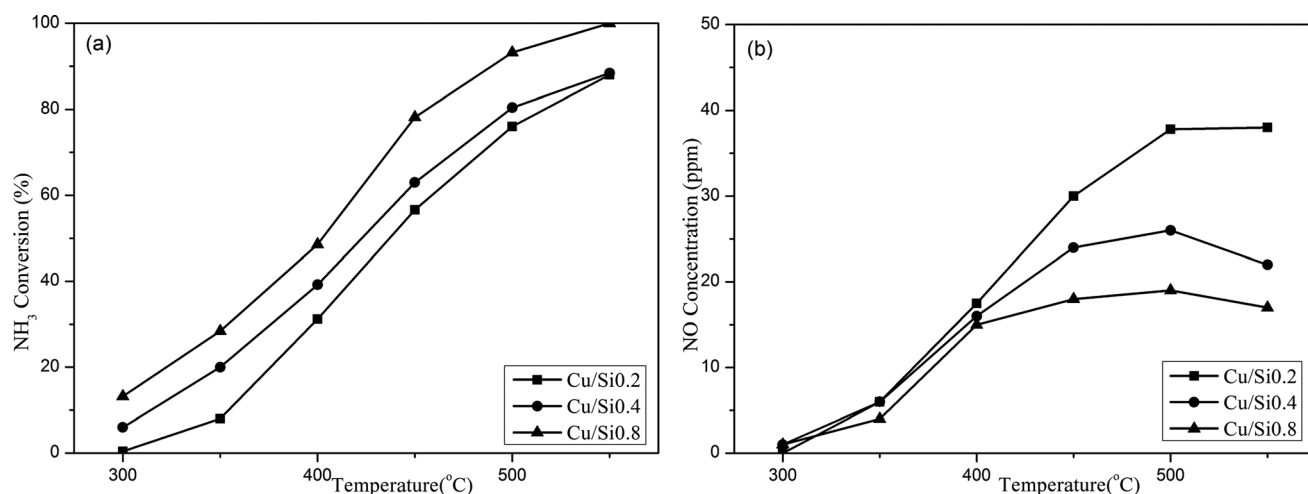


Fig. 9 The NH<sub>3</sub> oxidation activity over Cu/SAPO-34 catalysts. (a) NH<sub>3</sub> conversion; (b) NO generation. The inlets consisted of 500 ppm NH<sub>3</sub> and 5% O<sub>2</sub>, with N<sub>2</sub> as the balance. The volume hourly space velocity in the experiments was kept at 30 000 h<sup>-1</sup>.

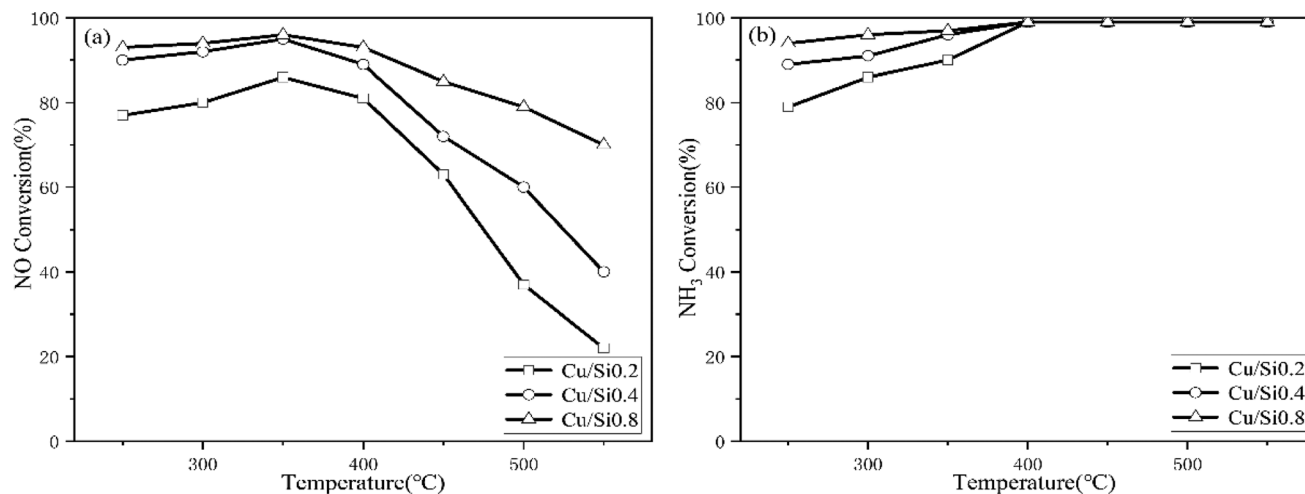


Fig. 10 The  $\text{NH}_3$  SCR activity over Cu/SAPO-34 catalysts. (a) NO conversion; (b)  $\text{NH}_3$  conversion. The inlets consisted of 500 ppm NO, 500 ppm  $\text{NH}_3$  and 5%  $\text{O}_2$ , with  $\text{N}_2$  as the balance. The volume hourly space velocity in the experiments was kept at  $30\,000\text{ h}^{-1}$ .

following the sequence as: Si0.2 ( $0.0043\text{ mmol g}^{-1}$ ) < Si0.4 ( $0.0091\text{ mmol g}^{-1}$ ) < Si0.8 ( $0.0197\text{ mmol g}^{-1}$ ). As the Si content increased, the peak point shifted towards higher temperatures, suggestive of an enhanced acid strength.

The  $\text{NH}_3$  conversion rates at  $300\text{ }^\circ\text{C}$  were calculated based on the data of  $\text{NH}_3$  oxidation steady-state tests, and the results were Si0.2 ( $0.039\text{ mmol s}^{-1}\text{ g}^{-1}$ ), Si0.4 ( $0.065\text{ mmol s}^{-1}\text{ g}^{-1}$ ) and Si0.8 ( $0.165\text{ mmol s}^{-1}\text{ g}^{-1}$ ) as shown in Fig. 6. It could be seen that the  $\text{NH}_3$  conversion rates at high temperature were proportional to the acidity of the samples, which indicated that the  $\text{NH}_3$  oxidation activity of the SAPO-34 support at high temperature was closely related to its strong structural Brønsted acid sites.

### 3.2 The $\text{NH}_3$ oxidation over the Cu/SAPO-34 catalysts

**3.2.1  $\text{H}_2$ -TPR results.** In order to further investigate the change of various copper species, the  $\text{H}_2$ -TPR tests were performed and the results were shown in Fig. 7. The  $\text{H}_2$  consumption signal from  $150\text{ }^\circ\text{C}$  to  $600\text{ }^\circ\text{C}$  was divided into three peaks after deconvolution and curve stochastic fitting procedures by Lorentzian method. The peak at the lower temperature (peak A) was assigned to the reduction of CuO species to  $\text{Cu}^0$  in the Cu/SAPO-34. The peak (peak B) represented the reduction of isolated  $\text{Cu}^{2+}$  to  $\text{Cu}^+$ , and the higher temperature (peak C) came from the reduction from  $\text{Cu}^+$  to  $\text{Cu}^0$ .<sup>27–30</sup> Furthermore, the Fig. 8 displayed the comparison results of relative intensity of each Cu species through integrating the individual reduction peaks in Fig. 7. The computing method of transforming peak areas to the amount of each Cu species was proposed in our previous work.<sup>12</sup> The results showed that the amount of isolated  $\text{Cu}^{2+}$  species increased with the increment of the Si content, while the isolated CuO amount followed irregular sequence.

**3.2.2 The  $\text{NH}_3$  oxidation and  $\text{NH}_3$  SCR activity over the Cu/SAPO-34 catalysts.** The Cu/SAPO-34 catalysts were prepared by impregnated method, and the Cu contents of each catalyst were all below 1%, (CuSi0.2, 0.76%; CuSi0.4, 0.98%; CuSi0.8, 0.74%) as shown in the Table 1. As shown in Fig. 9, the  $\text{NH}_3$  conversion

of Cu/Si0.8 was higher than the other two samples, and reached 100% at  $550\text{ }^\circ\text{C}$ . In the  $\text{NH}_3$  oxidation reaction, NO emerged as the primary by-product. Notably, the amount of NO produced on the Cu/SAPO-34 was significantly lower compared to that on the SAPO-34 supports.

For three catalysts in the Fig. 10, the  $\text{NH}_3$  SCR activity exhibited the following order during the  $250\text{--}550\text{ }^\circ\text{C}$ : Cu/Si0.2 < Cu/Si0.4 < Cu/Si0.8 in the Fig. 10a, and the Cu/Si0.8 shown the optimal SCR activity. Synchronously, the  $\text{NH}_3$  conversion followed the same pattern below  $400\text{ }^\circ\text{C}$  and their conversion rates are almost 100% above  $400\text{ }^\circ\text{C}$ .

**3.2.3 The kinetics tests over the Cu/SAPO-34 catalysts.** The kinetic test of  $\text{NH}_3$  oxidation reaction was performed from  $440\text{ }^\circ\text{C}$  to  $500\text{ }^\circ\text{C}$ , during which the  $\text{NH}_3$  conversion was less than 20%. In Fig. 11, the  $\text{NH}_3$  conversion rates rose with the increase of the Si content, explaining the  $\text{NH}_3$  conversion sequence in Fig. 9. Moreover, the three lines presented the equivalent slope,

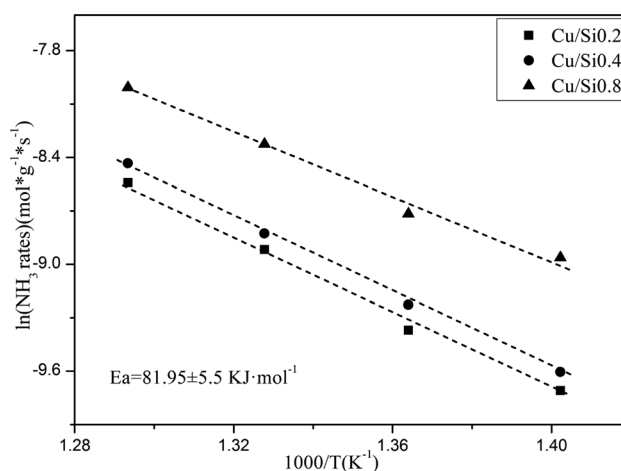
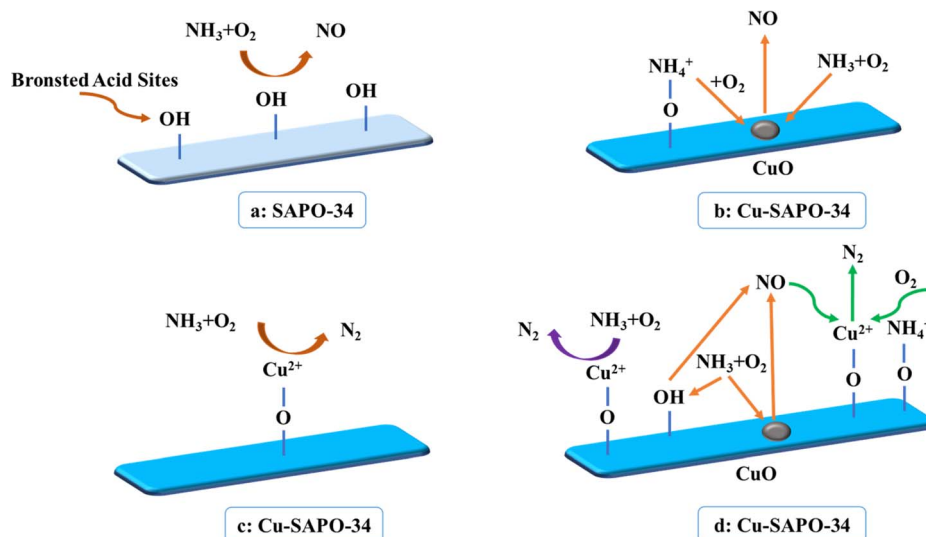


Fig. 11 The kinetic results of  $\text{NH}_3$  oxidation over the Cu/SAPO-34 catalysts. The inlets consisted of 500 ppm  $\text{NH}_3$  and 5%  $\text{O}_2$ , with  $\text{N}_2$  as the balance. The kinetic steady-state tests were conducted from  $440\text{ }^\circ\text{C}$  to  $500\text{ }^\circ\text{C}$ .





Scheme 1 The NH<sub>3</sub> oxidation mechanism of the SAPO-34 support and Cu/SAPO-34 catalyst.

indicating the same NH<sub>3</sub> oxidation mechanism over three catalysts as shown in Fig. 11. And the apparent activation energy ( $E_a$ ) for the NH<sub>3</sub> oxidation calculated from the slope was about 81.95 kJ mol<sup>-1</sup>.

Compared with NH<sub>3</sub> oxidation performance in Fig. 4 and 9, though three Cu/SAPO-34 samples exhibited the same rank of NH<sub>3</sub> conversion with their corresponding SAPO-34 supports, while the involved reaction mechanism were completely different. For SAPO-34 supports, only the Brønsted acid sites possessed the NH<sub>3</sub> oxidation activity, and the generated NO could not be consumed for no SCR active sites on neat support. Nevertheless, except the residual Brønsted acid sites, Cu/SAPO-34 also contained CuO species, which could further convert NH<sub>3</sub> into NO. But the presence of isolated Cu<sup>2+</sup> species could convert the NO into N<sub>2</sub> by NH<sub>3</sub> through the selective catalytic reduction (SCR) reaction, which declined NO release and synchronously improved NH<sub>3</sub> conversion. It has been widely reported that isolated Cu<sup>2+</sup> species are the active sites for NH<sub>3</sub>-SCR over Cu/SAPO-34, while CuO species are the most active sites for NH<sub>3</sub> oxidation.<sup>11,31</sup> The Fig. 10a and b revealed that Cu/Si0.8 presented the highest SCR performance and Cu/Si0.2 exhibited the lowest SCR performance, which just explained the rank of NH<sub>3</sub> conversion and NO concentration in Fig. 9a and b. And the tandem reaction of the front NH<sub>3</sub> oxidation and the back NH<sub>3</sub>-SCR induced the completely various products between the SAPO-34 and Cu/SAPO-34. In the meantime, it was seen that the sufficient strong acid sites and higher Cu<sup>2+</sup>/CuO ratios over Cu/SAPO-34 benefited N<sub>2</sub> as the main product for NH<sub>3</sub>-SCR and NH<sub>3</sub> oxidation reaction, but not NO, NO<sub>2</sub> or N<sub>2</sub>O.

### 3.3 The different NH<sub>3</sub> oxidation mechanism over the SAPO-34 and Cu/SAPO-34

Combining above results and discussion, we could conclude that the strong structural Brønsted acid sites were the NH<sub>3</sub> oxidation active sites of the SAPO-34 support, and the NH<sub>3</sub> reacts primarily with O<sub>2</sub> at these Brønsted acid sites, giving rise to the formation of NO as the main by-product. While the NH<sub>3</sub>

oxidation mechanism over the Cu/SAPO-34 catalyst was distinctly different due to the introduce of Cu species. It was proposed that the NH<sub>3</sub> oxidation mechanism over the Cu/SAPO-34 contained two steps. Firstly, NH<sub>3</sub> species reacted with O<sub>2</sub> on CuO sites and Brønsted acid sites to form NO products; and subsequently, the generated NO was reduced by NH<sub>3</sub> to N<sub>2</sub> on isolated Cu<sup>2+</sup> sites. Additionally, the isolated Cu<sup>2+</sup> sites have a crucial role in facilitating the NH<sub>3</sub> oxidation process to the production of N<sub>2</sub> as exhibited in the Scheme 1.

## 4. Conclusion

The impregnation method was used to synthesize the Cu/SAPO-34 catalyst, in which CuO was the dominated Cu species. Furthermore, a kinetic study on NH<sub>3</sub> oxidation was conducted, and the findings indicated that CuO species served as the active sites for the NH<sub>3</sub> oxidation process. In conclusion, the strong structural Brønsted acid sites were the NH<sub>3</sub> oxidation active site for the SAPO-34 support, and the NH<sub>3</sub> reacted with the O<sub>2</sub> on the Brønsted acid sites mainly to produce the NO. However, the NH<sub>3</sub> oxidation mechanism over the Cu/SAPO-34 catalyst was distinctly different due to the introduce of Cu species. It was proposed that the NH<sub>3</sub> oxidation mechanism over the Cu/SAPO-34 contained two steps: firstly, molecular NH<sub>3</sub> reacted with O<sub>2</sub> at CuO sites and residual Brønsted acid sites to form NO products; and subsequently, the generated NO was reduced by NH<sub>3</sub> to N<sub>2</sub> at isolated Cu<sup>2+</sup> sites. Meanwhile, the isolated Cu<sup>2+</sup> sites could show another crucial role in the NH<sub>3</sub> oxidation process that leads to the production of N<sub>2</sub>. Generally speaking, the desired NH<sub>3</sub>-SCR and NH<sub>3</sub> oxidation performance could be achieved simultaneously *via* the control of acidity and Cu species distribution on Cu/SAPO-34 catalysts.

## Conflicts of interest

There are no conflicts to declare.



## Acknowledgements

The authors would like to acknowledge the support of National Natural Science Foundation of China (22008195, 52102051), the PhD Research Start-up Fund Project of Xi'an University of Science and Technology (6310118004), Xi'an University of Science and Technology Research Training Fund (201704), Natural Science Basic Research Program of Shaanxi Province (2021JM-387), and the Postdoctoral Research Support Program of Xi'an University of Science and Technology.

## References

- 1 J. Wang, H. Zhao, G. Haller and Y. Li, *Appl. Catal., B*, 2017, **202**, 346–354.
- 2 C. Peng, R. Yan, H. Peng, Y. Mi, J. Liang, W. Liu, X. Wang, G. Song, P. Wu and F. Liu, *J. Hazard. Mater.*, 2020, **385**, 121593.
- 3 H. Wang, J. Jia, S. Liu, H. Chen, Y. Wei, Z. Wang, L. Zheng, Z. Wang and R. Zhang, *Environ. Sci. Technol.*, 2021, **55**, 5422–5434.
- 4 C. Zhong, J. Tan, H. Zuo, X. Wu, S. Wang and J. Liu, *Energy*, 2021, **230**, 120814.
- 5 Y. Zhao, B. Choi and D. Kim, *Chem. Eng. Sci.*, 2017, **164**, 258–269.
- 6 Y. Jung, Y. Pyo, J. Jang, Y. Woo, A. Ko, G. Kim, Y. Shin and C. Cho, *Fuel*, 2022, **310**, 122453.
- 7 S. Zhang, L. Pang, Z. Chen, S. Ming, Y. Dong, Q. Liu, P. Liu, W. Cai and T. Li, *Appl. Catal., A*, 2020, **607**, 117855.
- 8 X. Wang, M. Qin, Y. Xu and Q. Li, *J. Colloid Interface Sci.*, 2023, **638**, 686–694.
- 9 Z. Shi, Q. Peng, J. E. B. Xie, J. Wei, R. Yin and G. Fu, *Fuel*, 2023, **331**, 125885.
- 10 J. Fan, P. Ning, Y. Wang, Z. Song, X. Liu, H. Wang, J. Wang, L. Wang and Q. Zhang, *Chem. Eng. J.*, 2019, **369**, 908–919.
- 11 M. Jabłońska, *J. Mol. Catal.*, 2022, **518**, 112111.
- 12 J. Xue, X. Wang, G. Qi, J. Wang, M. Shen and W. Li, *J. Catal.*, 2013, **297**, 56–64.
- 13 T. Yu, J. Wang, M. Shen and W. Li, *Catal. Sci. Technol.*, 2013, **3**, 3234–3241.
- 14 M. Colombo, I. Nova, E. Tronconi, V. Schmeißer, B. Bandl-Konrad and L. Zimmermann, *Appl. Catal., B*, 2013, **142–143**, 861–876.
- 15 A. Ko, Y. Woo, J. Jang, Y. Jung, Y. Pyo, H. Jo, O. Lim and Y. J. Lee, *J. Ind. Eng. Chem.*, 2019, **78**, 433–439.
- 16 G. Liu, W. Bao, W. Zhang, D. Shen, Q. Wang, C. Li and K. H. Luo, *J. Energy Inst.*, 2019, **92**, 1262–1269.
- 17 P. N. R. Vennestrøm, A. Katerinopoulou, R. R. Tiruvalam, A. Kustov, P. G. Moses, P. Concepcion and A. Corma, *ACS Catal.*, 2013, **3**, 2158–2161.
- 18 L. Wang, J. R. Gaudet, W. Li and D. Weng, *J. Catal.*, 2013, **306**, 68–77.
- 19 S. Zhang, Y. Meng, K. Christian Kemp, C. Pan, Q. Ding, L. Pang, W. Cai and T. Li, *Chem. Eng. J.*, 2023, **452**, 139143.
- 20 X. Li, Y. Zhao, H. Zhao, M. Liu, Y. Ma, X. Yong, H. Chen and Y. Li, *Catal. Today*, 2019, **327**, 126–133.
- 21 J. Tan, Z. Liu, X. Bao, X. Liu, X. Han, C. He and R. Zhai, *Microporous Mesoporous Mater.*, 2002, **53**(1–3), 97–108.
- 22 L. Marchese, A. Frache, G. Gatti, S. Coluccia, L. Lisi, G. Ruoppolo, G. Russo and H. Pastore, *J. Catal.*, 2002, **208**, 479–484.
- 23 S. R. Venna and M. A. Carreon, *J. Phys. Chem. B*, 2008, **112**, 16261–16265.
- 24 F. Wang, L. Sun, C. Chen, Z. Chen, Z. Zhang, G. Wei and X. Jiang, *RSC Adv.*, 2014, **4**, 46093–46096.
- 25 B. Hari Babu, K. T. Venkateswara Rao, Y. W. Suh, P. S. Sai Prasad and N. Lingaiah, *New J. Chem.*, 2018, **42**, 1892–1901.
- 26 S. S. Acharyya, S. Ghosh, Y. Yoshida, T. Kaneko, T. Sasaki and Y. Iwasawa, *ACS Catal.*, 2021, **11**, 6698–6708.
- 27 S. S. Acharyya, S. Ghosh, R. Tiwari, C. Pendem, T. Sasaki and R. Bal, *ACS Catal.*, 2015, **5**, 2850–2858.
- 28 M. B. Gawande, A. Goswami, F.-X. Felpin, T. Asefa, X. Huang, R. Silva, X. Zou, R. Zboril and R. S. Varma, *Chem. Rev.*, 2016, **116**, 3722–3811.
- 29 D. L. Hoang, T. T. H. Dang, J. Engeldinger, M. Schneider, J. Radnik, M. Richter and A. Martin, *J. Solid State Chem.*, 2011, **184**, 1915–1923.
- 30 K. Sonobe, M. Tanabe, T. Imaoka, W.-J. Chun and K. Yamamoto, *Chem.–Eur. J.*, 2021, **27**, 8452–8456.
- 31 Y. Huang, J. Wang, T. Yu, S. Zhu, M. Shen, W. Li and J. Wang, *Catal. Sci. Technol.*, 2014, **4**(9), 3004–3012.

